MOLECULAR IMAGING AND BIOLOGY

Mol Imaging Biol (2018) 20:584–593
DOI: 10.1007/s11307-018-1161-7

Published Online: 19 January 2018

RESEARCH ARTICLE

Improving PET Quantification of Small Animal [^{68}Ga]DOTA-Labeled PET/CT Studies by Using a CT-Based Positron Range Correction

Jacobo Cal-Gonzalez,[1,2] Juan José Vaquero,[3,4] Joaquín L. Herraiz,[2] Mailyn Pérez-Liva,[2] María Luisa Soto-Montenegro,[4,5] Santiago Peña-Zalbidea,[3,4,6] Manuel Desco,[3,4,5,7] José Manuel Udías[2]

[1]*QIMP group, Center for Medical Physics and Biomedical Engineering, Medical University of Vienna, Vienna, Austria*
[2]*Grupo de Física Nuclear, Dpto. Física Atómica, Molecular y Nuclear, Universidad Complutense de Madrid, CEI Moncloa, Madrid, Spain*
[3]*Departamento de Bioingeniería e Ingeniería Aeroespacial, Universidad Carlos III de Madrid, Madrid, Spain*
[4]*Instituto de Investigación Sanitaria Gregorio Marañón, Madrid, Spain*
[5]*CIBERSAM, Madrid, Spain*
[6]*IRAB—Institut de Radiofarmàcia Aplicada de Barcelona (PRBB), Barcelona, Spain*
[7]*Centro Nacional de Investigaciones Cardiovasculares Carlos III (CNIC), Madrid, Spain*

Abstract

Purpose: Image quality of positron emission tomography (PET) tracers that emits high-energy positrons, such as Ga-68, Rb-82, or I-124, is significantly affected by positron range (PR) effects. PR effects are especially important in small animal PET studies, since they can limit spatial resolution and quantitative accuracy of the images. Since generators accessibility has made Ga-68 tracers wide available, the aim of this study is to show how the quantitative results of [^{68}Ga]DOTA-labeled PET/X-ray computed tomography (CT) imaging of neuroendocrine tumors in mice can be improved using positron range correction (PRC).

Procedures: Eighteen scans in 12 mice were evaluated, with three different models of tumors: PC12, AR42J, and meningiomas. In addition, three different [^{68}Ga]DOTA-labeled radiotracers were used to evaluate the PRC with different tracer distributions: [^{68}Ga]DOTANOC, [^{68}Ga]DOTATOC, and [^{68}Ga]DOTATATE. Two PRC methods were evaluated: a tissue-dependent (TD-PRC) and a tissue-dependent spatially-variant correction (TDSV-PRC). Taking a region in the liver as reference, the tissue-to-liver ratio values for tumor tissue (TLR_{tumor}), lung (TLR_{lung}), and necrotic areas within the tumors ($TLR_{necrotic}$) and their respective relative variations (ΔTLR) were evaluated.

Results: All TLR values in the PRC images were significantly different ($p < 0.05$) than the ones from non-PRC images. The relative differences of the tumor TLR values, respect to the case with no PRC, were ΔTLR_{tumor} 87 ± 41 % (TD-PRC) and 85 ± 46 % (TDSV-PRC). TLR_{lung} decreased when applying PRC, being this effect more remarkable for the TDSV-PRC method, with relative differences respect to no PRC: $\Delta TLR_{lung} = -45 \pm 24$ (TD-PRC), -55 ± 18 (TDSV-PRC). $TLR_{necrotic}$ values also decreased when using PRC, with more noticeable differences for TD-PRC: $\Delta TLR_{necrotic} = -52 \pm 6$ (TD-PRC), -48 ± 8 (TDSV-PRC).

Electronic supplementary material The online version of this article (https://doi.org/10.1007/s11307-018-1161-7) contains supplementary material, which is available to authorized users.

Correspondence to: Jacobo Cal-Gonzalez; *e-mail:* jacobo.calgonzalez@meduniwien.ac.at

Conclusion: The PRC methods proposed provide a significant quantitative improvement in [^{68}Ga]DOTA-labeled PET/CT imaging of mice with neuroendocrine tumors, hence demonstrating that these techniques could also ameliorate the deleterious effect of the positron range in clinical PET imaging.

Key words: [^{68}Ga]DOTA-labeled radiotracers, Positron range correction, Small animal PET/CT, PET image reconstruction

Introduction

With the extension of the positron emission tomography (PET) from clinical to preclinical research, it is possible to obtain preclinical PET images with sub-millimeter resolution and sensitivity close to 10 % [1]. Apart from the PET radionuclides more conventionally used such as F-18, C-11, and N-13, other radionuclides such as Ga-68, I-124, and Rb-82 have been proposed for PET imaging, with hundreds of PET radiotracers based on these radionuclides being developed [2].

[^{68}Ga]DOTA-labeled somatostatin analogues bind specifically to somatostatin receptors (SSTRs) and are commonly used for imaging and treatment planning of neuroendocrine tumors (NETs) [3–8]. Moreover, [^{68}Ga]DOTA-labeled somatostatin analogues have been reported to show higher sensitivity for the detection of NETs and other somatostatin-receptor expressing tumors than the most widely used radiotracer, 2-deoxy-2-[^{18}F]fluoro-D-glucose ([^{18}F]FDG), which is used to measure glucose metabolism [9–11]. This makes them ideally suited for this kind of tumors, which due to the availability of Ga-68 generators explain the wide spreading use of the these radionuclides during the last years.

However, obtaining accurate quantification and in general good quality images from Ga-68 PET is a challenging task [12–15]. The main concern lies with the high-energy positrons emitted by this radionuclide (see Table 1), which result in significant positron range (PR) effects affecting the spatial resolution of the PET images. PR effects are even more pronounced in high-resolution preclinical PET systems [18]. Figure 1 illustrates the degraded image quality due to the positron range effect when imaging Ga-68 based radiotracers. The figure shows simulated PET images of a NEMA NU4 image quality phantom [19] filled with respectively F-18 and Ga-68. As expected, a significant degradation of the quality of the images obtained with Ga-68 is observed, with lower spatial resolution and contrast, due to the larger positron range of the Ga-68 radionuclide. Therefore, an accurate correction of the PR effects is necessary to obtain good quantification for small animal images with Ga-68 radiotracers.

Indeed, the blurring effect of the PR may be described as a contribution to the system point spread function (PSF) [21, 22]. Several methodologies have been proposed to model PR effects during reconstruction. In a homogeneous medium, for example, this blurring can be considered as isotropic [23, 24] with a non-Gaussian shape with a sharp central cusp and relatively broad tails. Therefore, most correction techniques for PR make use of analytic space-invariant isotropic blurring kernels. This is computationally very efficient but it is only valid for cases where tracer uptake is surrounded by a homogeneous medium [22, 25, 26]. To address inhomogeneous media, space variant analytic kernels have been proposed [27–29]. However, this remains challenging due to the complexity and irregularity of tissue boundaries. An alternative approach to analytic models is the use of on-the-fly Monte Carlo (MC) simulations to model the interactions of positrons at tissue boundaries such as lung/soft tissue and soft tissue/bone interfaces [30], which can be extracted from X-ray computed tomography (CT) or magnetic resonance (MR) scans. In this process, the local tissue delineation can be considered and appropriate blurring kernels can be generated for each individual voxel.

In a previous work [31], we proposed a fully tissue-dependent and spatially variant positron range correction (PRC) method which uses analytical expressions for the PR blurring kernels, obtained from fits to Monte Carlo simulations [24]. The procedure takes into account the different materials that the positron travels by until it annihilates. This information is taken from co-registered CT images. The simulations and phantom experiments performed in [31] demonstrated that the proposed PRC yields artifact-free images with up to a factor two resolution recovery for medium-large positron range radionuclides like ^{68}Ga.

The aim of this work is to evaluate the previously developed PRC method in [^{68}Ga]DOTA-labeled PET/CT

Table 1.. Properties of the Ga-68 positron emitter, compared with the standard F-18. The half-life, mean, and maximum energies of the emitted positron ($E_{\beta mean}$, $E_{\beta max}$) have been obtained from [16], while the mean and maximum positron range values in water (R_{mean}, R_{max}) were obtained from [17]

Radionuclide	Half-life (min)	$E_{\beta mean}$ (keV)	$E_{\beta max}$ (keV)	R_{mean}—water (mm)	R_{max}—water (mm)
F-18	109.8	250	634	0.6	2.4
Ga-68	67.7	836	1899	2.9	8.2

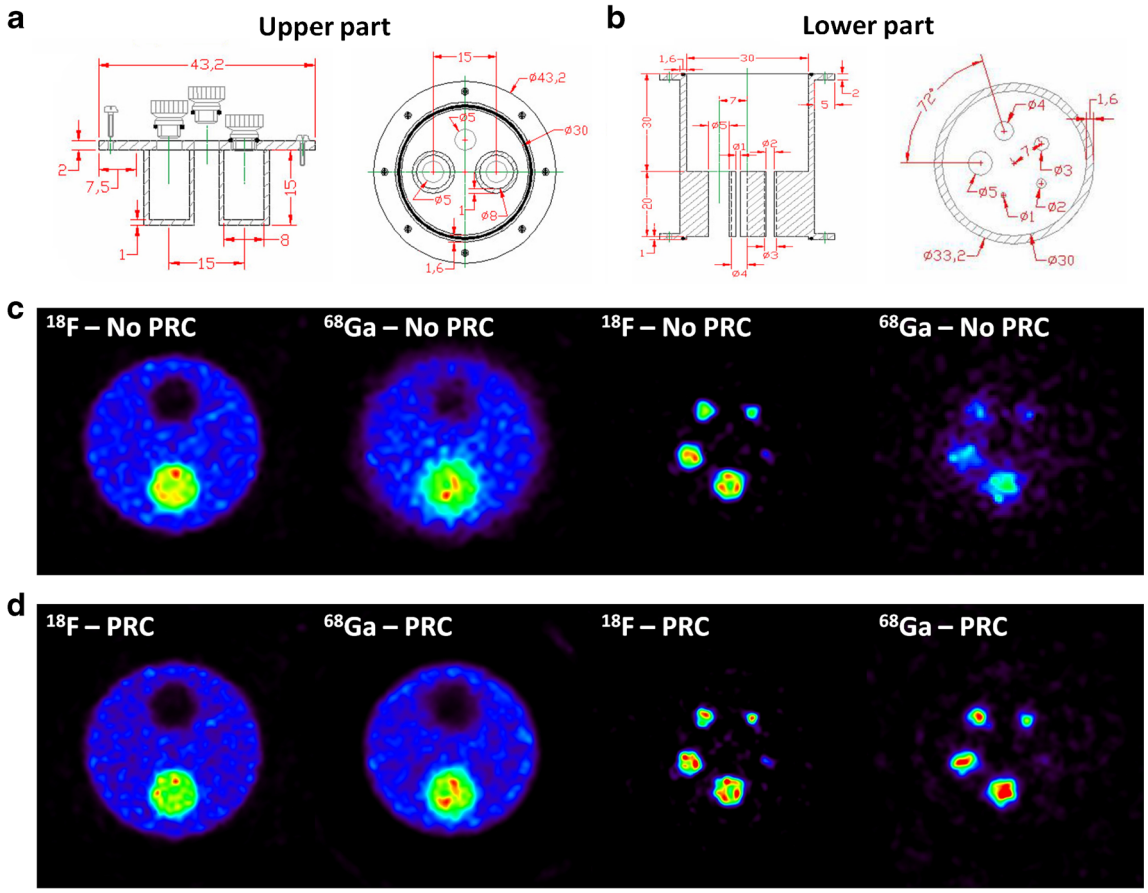

Fig. 1 The positron range effect when imaging a NEMA NU 4 image quality phantom [19] filled with Ga-68. In the top row of the figure, we show a schematic view of the **a** upper and **b** lower (right) parts of the phantom. **c** In the center row, we show transaxial views centered in these two parts, in simulated PET acquisitions of the phantom filled with F-18 and with Ga-68 and reconstructed with an standard OSEM algorithm without PRC. The differences in spatial resolution and contrast between the F-18 and Ga-68 images are due to the larger positron range of the Ga-68 radionuclide. **d** Finally, in the bottom row, we show the same images of the phantom, reconstructed with a tissue-dependent positron range correction (TD-PRC). For more details, we refer the reader to [20].

images of mice with neuroendocrine tumors and to show how the quantification of this highly demanding application can be improved by using the proposed PRC.

Materials and Methods

Animals

The experiments were performed using 12 male NUDE NU/NU mice. Animals were purchased from Charles River Laboratories (Spain), maintained at a constant temperature (24 ± 0.5 °C) under a 12-h light/dark cycle, and permitted access to commercial rodent laboratory chow and water *ad libitum*. All animal procedures were approved by the Animal Experimentation Ethics Committee of Hospital General Universitario Gregorio Marañón, Madrid, Spain, and were performed according to EU directive 2010/63/EU and national regulations (RD 53/2013).

Details about the cell culture, xenotransplantation, and the synthesis of the [68Ga]DOTA-peptides are available in the Electronic Supplementary Material (ESM).

Data Acquisition

Data were acquired with a high-resolution small-animal ARGUS PET-CT scanner (Sedecal, Spain) [32]. This tomograph has a transaxial and axial FOV of 68 and 48 mm respectively, and it is able of sub-millimetric resolution using iterative (PET) or direct 3D reconstruction (CT) [33, 34].

We evaluated 18 PET/CT scans. Imaging was performed between 7 and 53 days after tumor cell inoculation. Three different ^{68}Ga-based tracers were used in this work: [^{68}Ga]DOTATOC, [^{68}Ga]DOTANOC, and [^{68}Ga]DOTATATE. The tumor models and tracers were chosen to explore the performance of the proposed PRC method in a wide variety of cases with different tracer distributions.

Further details about the mice scans and the data acquisition (Suppl. Table 1) and reconstruction are provided in ESM.

Positron Range Correction

Two methods for PRC were evaluated in this work: a tissue-dependent (TD-PRC) and a tissue-dependent spatially-variant correction (TDSV-PRC). The PR blurring kernel is employed during the forward projection step in the iterative reconstruction procedure, as illustrated in Fig. 2. Details about the PRC methodology are provided in ESM.

Experimental Data Analysis

A reference region was located inside the liver of the mouse, defined as a cylinder of 3-mm diameter by 3-mm height. We evaluated the tissue-to-reference ratio values for several volumes of interest (VOIs): tumor tissue (TLR_{tumor}), lung (TLR_{lung}), and necrotic areas ($TLR_{necrotic}$), if the tumor presented a necrotic area with reduced uptake of the tracer. The segmentation of the tumor volume was performed from the PET images by drawing the 3D isocontour at 50 % of the maximum voxel value, measured from the TDSV-PRC PET images. The VOIs in lung and necrotic areas were defined as cylinders with the same size than the liver VOI. Figure 3 shows an example of the defined VOIs evaluated in this work, for a mouse with a tumor in which no necrotic area was observed (Fig. 3a) and for another mouse with necrotic area (Fig. 3b). All reconstructed images were evaluated at the same noise level. As the convergence speed of the OSEM algorithm with and without PRC is different, to ensure equal noise levels, the number of image updates in the reconstructed images used for the comparisons was higher in the non-PRC images than in the PRC images (see [20] and Table 2 for details).

To evaluate the effect of PRC methods on the quantification of the PET images, we calculated the relative changes in the evaluated tissue-to-background ratios (ΔTLR) after applying PRC. The ΔTLR was calculated as follows:

$$\Delta\mathrm{TLR}\ (\%) = \frac{\mathrm{TLR}\ (\mathrm{PRC}) - \mathrm{TLR}(noPRC)}{\mathrm{TLR}(noPRC)} \cdot 100 \qquad (1)$$

where *TLR(PRC)* is the tissue-to-background ratio after applying the PRC and *TLR(noPRC)* is the tissue-to-liver ratio measured in the image reconstructed without any PRC.

All TLR, noise, and ΔTLR values were reported as mean ± standard deviation (SD). One-way ANOVA and the Bonferroni test for means comparison were used to evaluate statistical significant changes in the TLR or noise values obtained without PRC, with TD-PRC, and with TDSV-PRC.

Results

Figure 4 shows the Ga-68 PET/CT images without PRC (left) and with TD (center) and TDSV (right) PRC of mice with implanted PC12, AR42J, and meningioma tumor models. The visual inspection of the images reveals a significant increase of the contrast of the images after applying PRC. Furthermore, a significant increase of the tracer uptake in the tumor is observed in all cases. Alternatively, Fig. 5 shows scans of the same mouse done at different stages of the tumor growth (7, 13, and 20 days after inoculation of meningioma tumor cells), with and without PRC. It is clear that at early stages (7 days), the small size of the tumor does not allow to see increased tumor uptake in the standard non-PRC reconstruction, while when PRC is incorporated into the reconstruction algorithm, a significant increase of tumor uptake can be observed. In later stages (13 and 20 days), necrotic areas appear within the tumors, and a significant improvement of the contrast in this area is appreciated when PRC is applied.

Table 2 shows mean, SD, and maximum and minimum values for TLR obtained for each of the VOIs evaluated. The table also presents mean noise values and number of

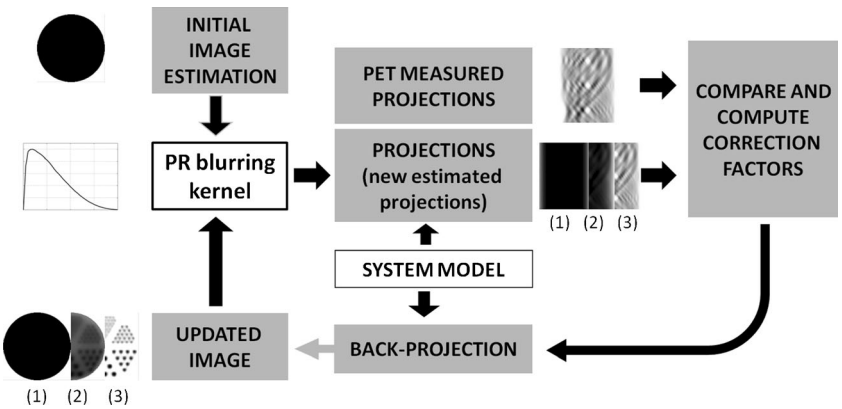

Fig. 2 The PRC method used in this work. The PR blurring kernel is modeled with Monte Carlo simulations and introduced into the reconstruction algorithm as an additional blurring to the image before the projection step in each iteration (1), (2), (3), *etc.* of the reconstruction algorithm.

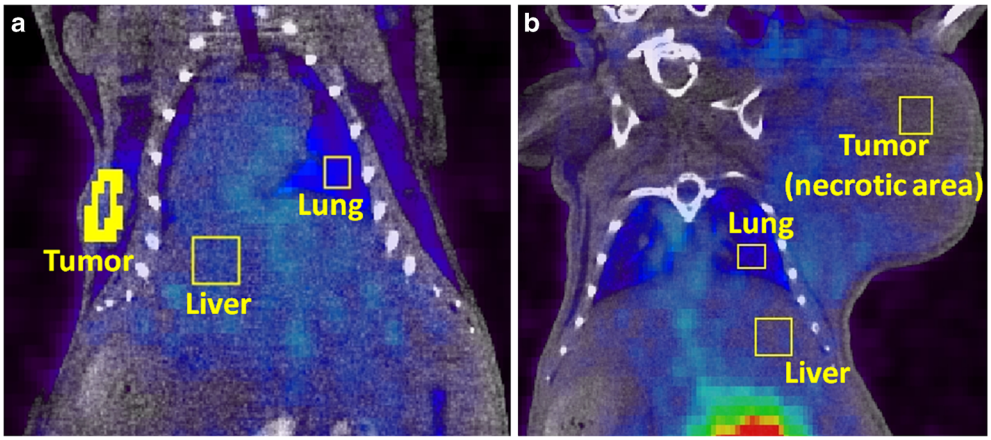

Fig. 3 Coronal views of the combined PET (color) and CT (gray scale) mice images. VOIs evaluated in this work, for a mouse with a tumor in which **a** no necrotic area was observed and **b** for a mouse with necrotic area. All the VOIs depicted in lung, liver, and necrotic areas were cylinders. The tumor VOIs were generated by using a threshold-based method to the 50 % of the maximum voxel value, measured from the PRC PET images.

iterations of the reconstructed image used for the evaluations. As mentioned above, due to the fact that PRC methods tend to increase the noise in the reconstructed images, we compared reconstructions at different number of iterations, with the aim of evaluating the different methods at the same noise level. Table 3 shows the mean and SD ΔTLR values for TD and TDSV PRC in all the VOIs evaluated and the *P* values obtained from the Bonferroni test. The mean ± SD relative change in noise and the correspondent *P* values are also shown in Table 3. With TD-PRC, we observed a mean increase of TLR_{tumor} values of 87 ± 41 %, while with TDSV-PRC, it was 85 ± 46 %. TLR_{lung} in general decreased when applying PRC, with more significant decreases with TDSV-PRC: mean $\Delta TLR_{lung} = -55 \pm 18$ %. $TLR_{necrotic}$ values also decreased when using PRC, but in this case, the difference is more noticeable for the TD-PRC: mean $\Delta TLR_{necrotic} = -52 \pm 6$ %. The contrast improvement of the images reconstructed with PRC is further demonstrated in Fig. 6, which presents box chart plots for TLR_{tumor}, TLR_{lung}, and $TLR_{necrotic}$, obtained from images reconstructed without PRC (No PRC), with tissue-dependent PRC (TD-PRC), and with tissue-dependent spatially-variant PRC (TDSV-PRC).

Discussion

In this work, we evaluated two different PRC methods in [^{68}Ga]DOTA-labeled PET/CT imaging of mice with implanted neuroendocrine tumors: a tissue-dependent correction (TD-PRC), which uses an isotropic spatially-invariant blurring kernel, and a tissue-dependent spatially-variant correction (TDSV-PRC), in which the different materials that the positron travels by until it annihilates are taken into account. Eighteen independent scans in 12 mice were evaluated, with three models of tumors and three [^{68}Ga]DOTA-labeled radiotracers, in order to evaluate the PRC performance in cases with different tracer distributions.

As expected, the relatively large PR of the Ga-68 radionuclide results in PET images with a significant reduced image quality, as illustrated in the example presented at Fig. 1. When using any of the proposed methods for PRC, we observed a noticeable improvement in the contrast of the reconstructed PET images (see Figs. 4, 5, and 6 and Tables 2 and 3) in all the cases.

In general, TDSV-PRC provides better results than TD-PRC. Although the TLR_{tumor} ($TLR_{necrotic}$) values obtained with the TD-PRC are slightly higher (lower) than the ones obtained with TDSV-PRC; these differences are very small, not statistically significant at a

Table 2.. Mean, SD, and maximum and minimum values for the TLR obtained in each VOIs. Bottom row: mean noise values and mean number of image updates of the reconstructed image used for the evaluations. Due to the different convergence properties of the PRC and no-PRC reconstruction algorithms, we aimed to compare images at the same level of noise, and in consequence, with different number of image updates in the iterative algorithms [20, 31]

	N total	No PRC		TD-PRC		TDSV-PRC	
		Mean ± SD	Range	Mean ± SD	Range	Mean ± SD	Range
TLR_{tumor}	22	1.6 ± 0.6	0.88–3.35	3.0 ± 1.4	1.40–6.57	3.0 ± 1.7	1.34–7.54
TLR_{lung}	18	0.62 ± 0.22	0.21–1.02	0.36 ± 0.21	0.04–0.75	0.29 ± 0.17	0.05–0.58
$TLR_{necrotic}$	7	0.46 ± 0.16	0.29–0.78	0.22 ± 0.08	0.13–0.39	0.24 ± 0.09	0.13–0.41
Noise (%)	18	14.9 ± 3.8	11.5–28.0	14.7 ± 4.3	10.3–29.3	14.8 ± 4.3	10.4–29.1
(#Image updates)		150 to 200		100		100	

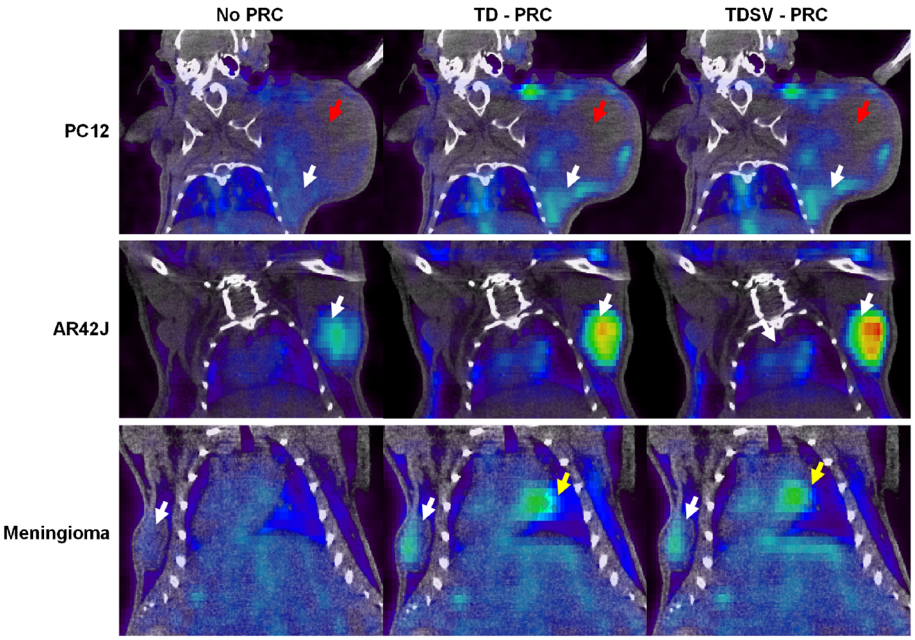

Fig. 4 [^{68}Ga]DOTA-labeled PET/CT images without (left), with TD (center), and with TDSV (right) PRC of mice with implanted PC12, AR42J, and meningioma tumor cells. White arrows point to tumor regions with increased tracer uptake, while red arrows (top) point to necrotic areas in the tumor, with reduced tracer uptake. The yellow arrows on the bottom point to an artifact in which the heart uptake is wrongly co-registered with heart tissue (TD-PRC image). This is due to an over correction of the PR effect in the voxels close to the heart, where there is lung tissue, and therefore, a kernel blurring corresponding to lung is used in the TD-PRC, but the lung-heart boundary significant reduces the PR kernel in this direction. When the TDSV-PRC is used, the heart uptake is correctly co-registered with heart tissue. Note that the tumor with necrotic area (PC12) corresponds to mouse 3, which was scanned 53 days after inoculation of the tumor cells.

confidence level of 5 %, as shown in Table 3. However, a noticeable smaller TLR_{lung} was obtained with TDSV-PRC. In addition, artificially increased uptakes at the edges of the animal bodies were observed when using the TD-PRC, due to the wrong blurring kernels used by this method at these regions, namely, homogeneous kernels using tissue as reference in voxels within the body, when inhomogeneous kernels accounting for the boundary tissue-air should be used.

A general limitation of the proposed PRC methods is the increase of noise in the image due to the positron range blurring kernel deconvolution being applied only in the

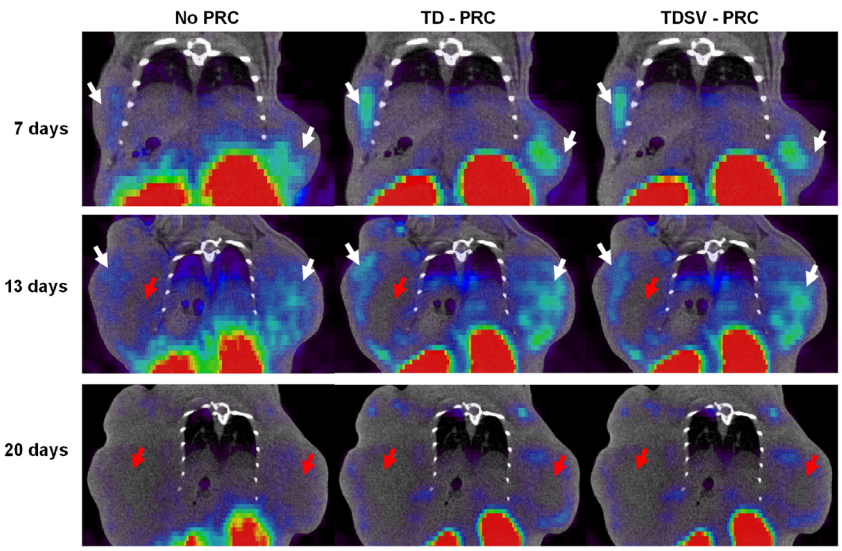

Fig. 5 Scans of the same mouse, performed at different stages of the tumor growth: 7, 13, and 20 days after the inoculation of meningioma tumor cells. The PET images were reconstructed without (left), with TD (center), and with TDSV (right) PRC. White arrows point to active areas of the tumors, with increased [^{68}Ga]DOTATATE uptake, while red arrows point to necrotic areas of the tumors.

Table 3.. Mean, SD, and (minimum, maximum) values for the ΔTLR obtained in each evaluated VOIs. Bottom row: mean, SD, and (minimum, maximum) Δnoise values. The *P* values for the statistically different means (Bonferroni test, 5 % confidence level) are also shown in the table. *NS* not significant statistical differences

	N total	TD - PRC			TDSV - PRC			
		Mean ± SD	Range	*P* (No PRC)	Mean ± SD	Range	*P* (No PRC)	*P* (TD-PRC)
ΔTLR_{tumor} (%)	22	87 ± 41	(37, 195)	0.003	85 ± 46	(31, 208)	0.002	NS
ΔTLR_{lung} (%)	18	−45 ± 24	(−81, 0)	< 0.001	−55 ± 18	(−78, −16)	< 0.001	NS
$\Delta TLR_{necrotic}$ (%)	7	−52 ± 6	(−61, −44)	0.004	−48 ± 8	(−61, −40)	0.007	NS
ΔNoise (%)	18	−0.8 ± 3.0	(−7, 5)	NS	0.4 ± 3.7	(−6, 7)	NS	NS

forward projection [28]. In this work, we have taken this issue into account by evaluating PRC and no-PRC images reconstructed at different number of image updates, in order to obtain similar noise values in both PRC and no-PRC

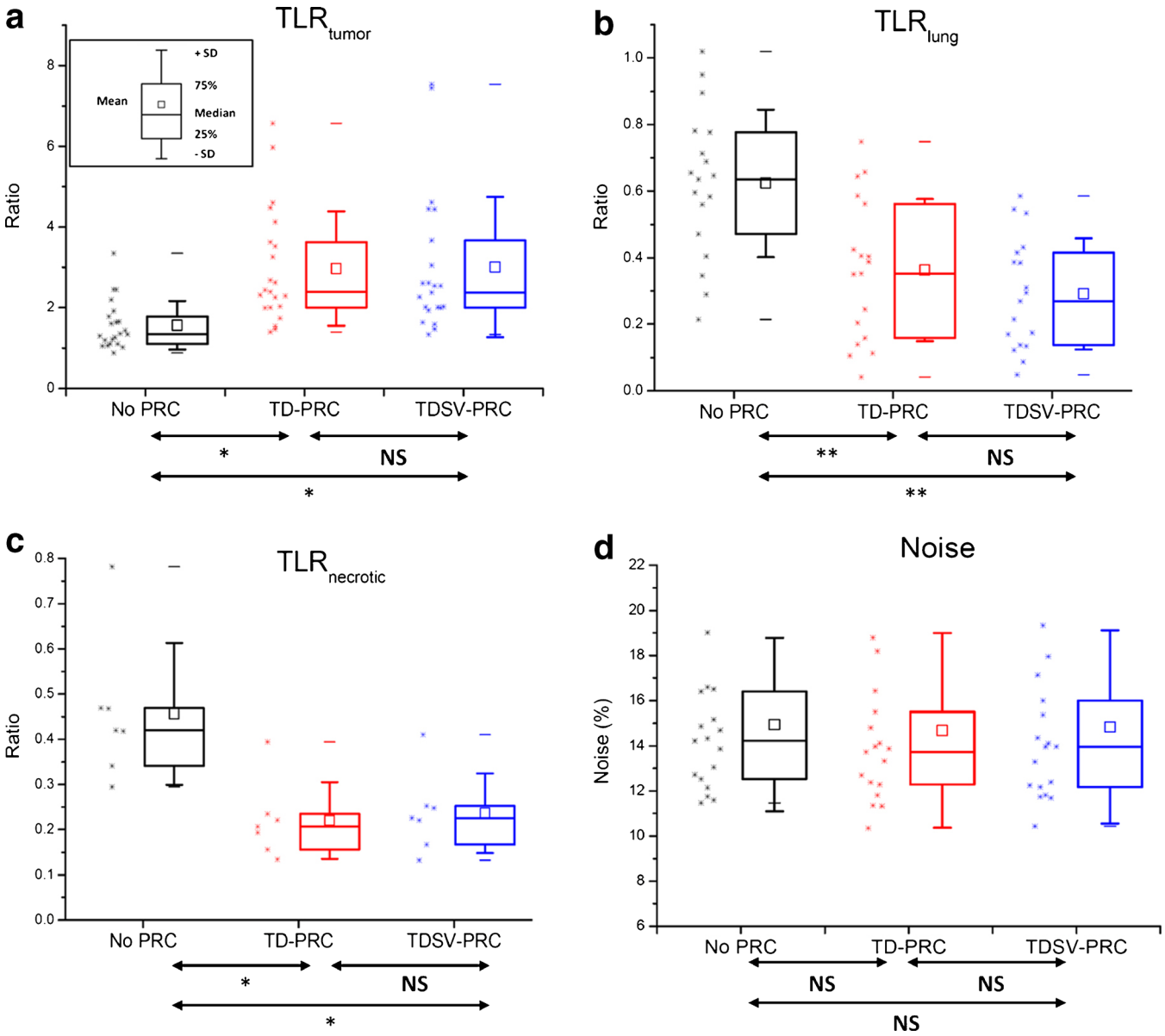

Fig. 6 **a** TLR_{tumor}, **b** TLR_{lung}, **c** $TLR_{necrotic}$, and **d** noise values obtained from the images reconstructed without PRC (No PRC), with TD PRC, and with TDSV-PRC. NS not significant statistical differences in the means (Bonferroni test, 5 % confidence level). *Statistically significant differences at 5 % confidence level ($0.05 > P > 0.001$). **Statistically significant differences at 0.1 % confidence level ($P < 0.001$).

images (see Table 3). Several approaches to overcome the noise limitation of PRC methods have been evaluated in the literature, such as using a maximum-a-posteriori (MAP) regularization in the image reconstruction process [26, 28] or introducing the positron range blurring kernel also in the back-projection step. This additional step leads to slower convergence of the reconstruction algorithm, as discussed in [20]. Although it is known that the mismatch between forward and backward projectors can exhibit problems in some cases [35], in general, using a less accurate backward projector is safe, provided that the forward projector contains all the relevant blurring effects, as discussed in [36, 37]. In our case, if PR is modeled also in the back-projection stage, we find essentially the same images, but the reconstruction process needs more number of iterations and takes longer. A full evaluation of the performance of the reconstruction algorithm with TDSV-PRC in both forward and backward projectors is out of the scope of this paper and it is going to be performed in future work.

As discussed in [31], the computation of the TDSV blurring kernel adds a manageable overhead to the overall reconstruction time, comparing with the TD correction. However, even for large-range isotopes, the computation time must not be considered as a limitation for preclinical applications. In the [^{68}Ga]DOTA-labeled studies considered in this work, the TDSV-PRC OSEM reconstruction using two iterations and 50 subsets took about 60 min in a single-core Intel Xeon @ 3.0 GHz. By using an open-MP parallel implementation of the code in eight cores this time can be reduced up to less than 10 min. This computation time is faster than other proposed PRC methods based on on-the-fly Monte Carlo estimations of positron range, since even if the PRC is applied as a residual correction after a given number of image updates, like in [30], at least one full Monte Carlo simulation is needed during the reconstruction process, which is more computationally demanding than our calculation of the TDSV blurring, which is performed only once at the beginning of the reconstruction.

Implications of This Work and Future Research

The results presented in this paper, together with the validations presented in [31], demonstrate that the quantitative evaluation of small animal PET images obtained with ^{68}Ga-DOTA-labeled radiotracers is improved when using appropriate PRC. This improved quantification can increase the diagnostic value of ^{68}Ga radiotracers, already established or under development [5, 38–40]. This would also apply to any preclinical study performed using radiotracers based on medium-large positron range radionuclides, such as O-15, I-124, or Rb-82 [41–44].

Although the most critical image degradation of the PET images due to positron range is seen in high-resolution small-animal imaging, this effect can also be relevant in clinical PET studies. For example, it is known that myocardial perfusion studies with ^{82}Rb suffer from significant resolution degradation mainly due to the large PR of Rb-82 (5.9 mm [17]). Only a few works have tried to improve the quantitative properties of this kind of studies by means of PRC [26, 27, 45]. Alternatively, Abdul-Fatah and colleagues [46] identified shine-trough artifacts when imaging thyroid tumors in the trachea with I-124 PET/CT due to its large PR. This effect may be even more important in PET/MR, when the high magnetic field in the axial axis creates an elongation of the PR in that direction [47, 48], as recently discussed by Kolb and colleagues [49]. To the best of our knowledge, these issues are still not solved. The implementation of our TDSV-PRC method in clinical PET/MR systems by means of an accurate 3D modeling of the PR kernel in magnetic fields is work in progress.

Conclusion

The proposed PRC methods provide high-resolution PET images with a significant quantitative improvement in [^{68}Ga]DOTA-labeled PET/CT imaging of mice with neuroendocrine tumors. Furthermore, the TDSV-PRC method results in accurate images free of artifacts in the tissue boundaries and with better contrast than the more simplistic TD-PRC. The results presented in this paper reveal a significant importance of performing an accurate PRC for the quantitative evaluation of small animal PET images obtained with medium-large positron range radionuclides. Clinical studies with large-range nuclides (cardiac Rb-82) or cases in which the lesion of interest is close to a tissue boundary (thyroid tumors) would also benefit of TDSV-PRC.

Acknowledgments. Open access funding provided by Medical University of Vienna. We acknowledge A. de Francisco and Y. Sierra for their skillful support during the imaging sessions, Randy Jenssen of the University of Utah for providing the CH-157MN meningioma cells, and BCN Peptides for providing somatostatin analogues.
The CNIC is supported by the Ministry of Economy, Industry and Competitiveness (MEIC) and the Pro CNIC Foundation, and is a Severo Ochoa Center of Excellence (SEV-2015-0505).

*Funding Information*This work was partially funded by the projects RTC-2015-3772-1, TEC2014-56600-R, and TEC2016-78052-R from the Spanish Ministry of Science and Innovation, Spanish Government, Spanish Ministry of Economy and Competitiveness grants (FIS PI11/00616, FIS PI14/00860, CP08/00017, and CPII14/00005) co-financed by European Regional Development Fund (ERDF), Alicia Koplowitz Foundation and TOPUS S2013/MIT-3024 project from the regional government of Madrid. The research leading to these results has received funding from the Innovative Medicines Initiative (www.imi.europa.eu) Joint Undertaking under grant agreement n°115337, resources of which are composed of financial contribution from the European Union's Seventh Framework Programme (FP7/2007-2013) and EFPIA companies' in kind contribution. Part of the calculations were performed in the "Clúster de Cálculo de Alta Capacidad para Técnicas Físicas" funded by UCM and by UE under the FEDER programme.

Compliance with Ethical Standards

All animal procedures were approved by the Animal Experimentation Ethics Committee of Hospital General Universitario Gregorio Marañón, Madrid,

Spain, and were performed according to EU directive 2010/63/EU and national regulations (RD 53/2013).

Conflict of Interest

The authors declare that they have no conflict of interest.

References

1. Goertzen AL, Bao Q, Bergeron M, Blankemeyer E, Blinder S, Canadas M, Chatziioannou AF, Dinelle K, Elhami E, Jans HS, Lage E, Lecomte R, Sossi V, Surti S, Tai YC, Vaquero JJ, Vicente E, Williams d, Laforest R (2012) NEMA NU 4-2008 comparison of preclinical PET imaging systems. J Nucl Med 53(8):1300–1309. https://doi.org/10.2967/jnumed.111.099382
2. MICAD Molecular Imaging and Contrast Agent Database (MICAD) [Internet]. Bethesda (MD): National Center for Biotechnology Information (US); 2004–2013. PET. Available from: https://www.ncbi.nlm.nih.gov/books/NBK22999/
3. Todorović-Tirnanić MV, Gajić MM, Obradović VB, Baum RP (2014) Gallium-68 DOTATOC PET/CT *in vivo* characterization of somatostatin receptor expression in the prostate. Cancer Biother Radiopharm 29(3):108–115. https://doi.org/10.1089/cbr.2013.1570
4. Kagna O, Pirmisashvili N, Tshori S, Freedman N, Israel O, Krausz Y (2014) Neuroendocrine tumor imaging with 68Ga-DOTA-NOC: physiologic and benign variants. AJR Am J Roentgenol 203(6):1317–1323. https://doi.org/10.2214/AJR.14.12588
5. Soto-Montenegro ML, Peña-Zalbidea S, Mateos-Pérez JM, Oteo M, Romero E, Morcillo MÁ, Desco M (2014) Meningiomas: a comparative study of 68Ga-DOTATOC, 68Ga-DOTANOC and 68Ga-DOTATATE for molecular imaging in mice. PLoS One 9(11):e111624. https://doi.org/10.1371/journal.pone.0111624
6. Combs SE, Welzel T, Habermehl D, Rieken S, Dittmar JO, Kessel K, Jäkel O, Haberkorn U, Debus J (2013) Prospective evaluation of early treatment outcome in patients with meningiomas treated with particle therapy based on target volume definition with MRI and 68Ga-DOTATOC-PET. Acta Oncol (Madr) 52(3):514–520. https://doi.org/10.3109/0284186X.2013.762996
7. Graf R, Nyuyki F, Steffen IG, Michel R, Fahdt D, Wust P, Brenner W, Budach V, Wurm R, Plotkin M (2013) Contribution of 68Ga-DOTATOC PET/CT to target volume delineation of skull base meningiomas treated with stereotactic radiation therapy. Int J Radiat Oncol Biol Phys 85(1):68–73. https://doi.org/10.1016/j.ijrobp.2012.03.021
8. Yılmaz S, Ocak M, Asa S et al (2012) Appearance of intracranial meningioma in FDG and 68Ga-DOTATOC PET/CT. Rev Esp Med Nucl Imagen Mol 32:60–61
9. Kuyumcu S, Özkan ZG, Sanli Y, Yilmaz E, Mudun A, Adalet I, Unal S (2013) Physiological and tumoral uptake of 68Ga-DOTATATE: standardized uptake values and challenges in interpretation. Ann Nucl Med 27(6):538–545. https://doi.org/10.1007/s12149-013-0718-4
10. Prasad V, Baum RP (2010) Biodistribution of the Ga-68 labeled somatostatin analogue DOTA-NOC in patients with neuroendocrine tumors: characterization of uptake in normal organs and tumor lesions. Q J Nucl Med Mol Imaging 54(1):61–67
11. Nilica B, Waitz D, Stevanovic V, Uprimny C, Kendler D, Buxbaum S, Warwitz B, Gerardo L, Henninger B, Virgolini I, Rodrigues M (2016) Direct comparison of 68Ga-DOTA-TOC and 18F-FDG PET/CT in the follow-up of patients with neuroendocrine tumour treated with the first full peptide receptor radionuclide therapy cycle. Eur J Nucl Med Mol Imaging 43(9):1585–1592. https://doi.org/10.1007/s00259-016-3328-2
12. Laforest R, Rowland DJ, Welch MJ (2002) MicroPET imaging with nonconventional isotopes. IEEE Trans Nucl Sci 49(I):2119–2126. https://doi.org/10.1109/TNS.2002.803685
13. Laforest R, Liu X (2008) Image quality with non-standard nuclides in PET. Q J Nucl Med Mol Imaging 52(2):151–158
14. Liu X, Laforest R (2009) Quantitative small animal PET imaging with nonconventional nuclides. Nucl Med Biol 36(5):551–559. https://doi.org/10.1016/j.nucmedbio.2009.01.019
15. Disselhorst JA, Brom M, Laverman P, Slump CH, Boerman OC, Oyen WJG, Gotthardt M, Visser EP (2010) Image-quality assessment for several positron emitters using the NEMA NU 4-2008 standards in the Siemens Inveon small-animal PET scanner. J Nucl Med 51(4):610–617. https://doi.org/10.2967/jnumed.109.068858
16. National Nuclear Data Center (NNDC) (2016) Chart of Nuclides - Decay Radiation. http://www.nndc.bnl.gov/
17. Bailey DL, Karp JS, Surti S (2005) Physics and instrumentation in PET. In: Bailey DL, Townsend DW, Valk PE, Maisey MN (eds) Positron emission tomography: basic sciences. Springer, London, pp 13–40. https://doi.org/10.1007/1-84628-007-9_2
18. Levin CS, Hoffman EJ (1999) Calculation of positron range and its effect on the fundamental limit of positron emission tomography system spatial resolution. Phys Med Biol 44(3):781–799. https://doi.org/10.1088/0031-9155/44/3/019
19. NEMA-NU-4. Performance measurements for small animal positron emission tomographs. Technical report, National Electrical Manufacturers Association, 2008
20. Cal-González J, Herraiz JL, España S et al (2011) Study of CT-based positron range correction in high resolution 3D PET imaging. Nucl Instruments Methods Phys Res Sect A Accel Spectrometers, Detect Assoc Equip 648:172–175
21. Derenzo SE (1986) Mathematical removal of positron range blurring in high resolution tomography. IEEE Trans Nucl Sci 33(1):565–569. https://doi.org/10.1109/TNS.1986.4337166
22. Haber SF, Derenzo SE, Uber D (1990) Application of mathematical removal of positron range blurring inpositron emission tomography IEEE Trans. Nucl Sci 37:371293–371299
23. Moses WW (2011) Fundamental limits of spatial resolution in PET. Nucl Instruments Methods Phys Res Sect A Accel Spectrometers, Detect Assoc Equip 648:S236–S240. https://doi.org/10.1016/j.nima.2010.11.092
24. Cal-González J, Herraiz JL, España S, Corzo PMG, Vaquero JJ, Desco M, Udias JM (2013) Positron range estimations with PeneloPET. Phys Med Biol 58(15):5127–5152. https://doi.org/10.1088/0031-9155/58/15/5127
25. Palmer MR, Xuping Z, Parker JA (2005) Modeling and simulation of positron range effects for high resolution PET imaging. IEEE Trans Nucl Sci 52(5):1391–1395. https://doi.org/10.1109/TNS.2005.858264
26. Rahmim A, Lodge MA, Tang J et al (2008) Analytic system matrix resolution modeling in PET: an application to Rb-82 cardiac imaging. Phys Med Biol 53(21):5947–5965. https://doi.org/10.1088/0031-9155/53/21/004
27. Alessio A, Macdonald L (2008) Spatially variant positron range modeling derived from CT for PET image reconstruction. IEEE Nucl Sci Symp Conf Rec :3637–3640
28. Bai B, Laforest R, Smith AM, Leahy RM (2005) Evaluation of MAP image reconstruction with positron range modeling for 3D PET. IEEE Nucl Sci Symp Conf Rec 5:2686–2689
29. Rahmim A, Tang J, Lodge MA, et al (2008) Resolution modeled PET image reconstruction incorporating space-variance of positron range: rubidium-82 cardiac PET imaging. IEEE Nucl Sci Symp Conf Rec :3643–3650
30. Fu L, Qi J (2010) A residual correction method for high-resolution PET reconstruction with application to on-the-fly Monte Carlo based model of positron range. Med Phys 37(2):704–713. https://doi.org/10.1118/1.3284980
31. Cal-Gonzalez J, Perez-Liva M, Herraiz JL, Vaquero JJ, Desco M, Udias JM (2015) Tissue-dependent and spatially-variant positron range correction in 3D PET. IEEE Trans Med Imaging 34(11):2394–2403. https://doi.org/10.1109/TMI.2015.2436711
32. Wang Y, Seidel J, Tsui BMW et al (2006) Performance evaluation of the GE healthcare eXplore VISTA dual-ring small-animal PET scanner. J Nucl Med 47(11):1891–1900
33. Herraiz JL, España S, Vaquero JJ, Desco M, Udías JM (2006) FIRST: fast iterative reconstruction software for (PET) tomography. Phys Med Biol 51(18):4547–4565. https://doi.org/10.1088/0031-9155/51/18/007
34. Abella M, Vaquero JJ, Sisniega A, Pascau J, Udías A, García V, Vidal I, Desco M (2012) Software architecture for multi-bed FDK-based reconstruction in X-ray CT scanners. Comput Methods Prog Biomed 107(2):218–232. https://doi.org/10.1016/j.cmpb.2011.06.008

35. Rahmim A, Cheng J-C, Dinelle K, Shilov M, Segars WP, Rousset OG, Tsui BMW, Wong DF, Sossi V (2008) System matrix modelling of externally tracked motion. Nucl Med Commun 29(6):574–581. https://doi.org/10.1097/MNM.0b013e3282f5d2de
36. Zeng GL, Gullberg GT (2000) Unmatched projector/backprojector pairs in an iterative reconstruction algorithm. IEEE Trans Med Imaging 19(5):548–555. https://doi.org/10.1109/42.870265
37. Kamphuis C, Beekman FJ, van Rijk PP, Viergever MA (1998) Dual matrix ordered subsets reconstruction for accelerated 3D scatter compensation in single-photon emission tomography. Eur J Nucl Med 25(1):8–18
38. Mathias CJ, Lewis MR, Reichert DE, Laforest R, Sharp TL, Lewis JS, Yang ZF, Waters DJ, Snyder PW, Low PS, Welch MJ, Green MA (2003) Preparation of 66Ga- and 68Ga-labeled Ga(III)-deferoxamine-folate as potential folate-receptor-targeted PET radiopharmaceuticals. Nucl Med Biol 30(7):725–731. https://doi.org/10.1016/S0969-8051(03)00080-5
39. Müller C (2013) Folate-based radiotracers for PET imaging—update and perspectives. Molecules 18(5):5005–5031. https://doi.org/10.3390/molecules18055005
40. Fani M, Wang X, Nicolas G, Medina C, Raynal I, Port M, Maecke HR (2011) Development of new folate-based PET radiotracers: preclinical evaluation of 68 Ga-DOTA-folate conjugates. Eur J Nucl Med Mol Imaging 38(1):108–119. https://doi.org/10.1007/s00259-010-1597-8
41. Wehrl HF, Martirosian P, Schick F, Reischl G, Pichler BJ (2014) Assessment of rodent brain activity using combined [15O]H2O-PET and BOLD-fMRI. NeuroImage 89:271–279. https://doi.org/10.1016/j.neuroimage.2013.11.044
42. Lee C-L, Wahnishe H, Sayre GA, Cho HM, Kim HJ, Hernandez-Pampaloni M, Hawkins RA, Dannoon SF, VanBrocklin HF, Itsara M, Weiss WA, Yang X, Haas-Kogan d, Matthay KK, Seo Y (2010) Radiation dose estimation using preclinical imaging with 124I-metaiodobenzylguanidine (MIBG) PET. Med Phys 37(9):4861–4867. https://doi.org/10.1118/1.3480965
43. Aljammaz I, Al-Otaibi B, Al-Hokbany N, Amer S, Okarvi S (2014) Development and pre-clinical evaluation of new 68Ga-NOTA-folate conjugates for PET imaging of folate receptor-positive tumors. Anticancer Res 34(11):6547–6556
44. Clemmensen AE, Ghotbi AA, Bodholdt RP et al (2016) Perfusion imaging using rubidium-82 (82Rb) PET in rats with myocardial infarction: first small animal cardiac 82Rb-PET. J Nucl Cardiol 82:1–3
45. Johnson NP, Sdringola S, Gould KL (2011) Partial volume correction incorporating Rb-82 positron range for quantitative myocardial perfusion PET based on systolic-diastolic activity ratios and phantom measurements. J Nucl Cardiol 18(2):247–258. https://doi.org/10.1007/s12350-010-9327-y
46. Abdul-Fatah SB, Zamburlini M, Halders SGEA, Brans B, Teule GJJ, Kemerink GJ (2009) Identification of a shine-through artifact in the trachea with 124 I PET/CT. J Nucl Med 50(6):909–911. https://doi.org/10.2967/jnumed.108.060442
47. Kraus R, Delso G, Ziegler SI (2012) Simulation study of tissue-specific positron range correction for the new biograph mMR whole-body PET/MR system. IEEE Trans Nucl Sci 59(5):1900–1909. https://doi.org/10.1109/TNS.2012.2207436
48. Cheng J, Boellaard R, Laforest R (2015) Evaluation of the effect of magnetic field on PET spatial resolution and contrast recovery using clinical PET scanners and EGSnrc simulations. IEEE Trans Nucl Sci 62(1):101–110. https://doi.org/10.1109/TNS.2014.2373147
49. Kolb A, Sauter AW, Eriksson L, Vandenbrouke A, Liu CC, Levin C, Pichler BJ, Rafecas M (2015) Shine-through in PET/MR imaging: effects of the magnetic field on positron range and subsequent image artifacts. J Nucl Med 56(6):951–954. https://doi.org/10.2967/jnumed.114.147637